

Geochemistry, Geophysics, Geosystems®



RESEARCH ARTICLE

10.1029/2024GC011827

On the Influence of Pressure, Phase Transitions, and Water on Large-Scale Seismic Anisotropy Underneath a Subduction Zone

John Keith Magali^{1,2} , Christine Thomas^{1,3} , Estelle Elisa Ledoux⁴, Yann Capdeville⁵ , and Sébastien Merkel² 

¹Institute of Geophysics, University of Münster, Münster, Germany, ²Université de Lille, CNRS, INRAE, Centrale Lille, UMR 8207—UMET—Unité Matériaux et Transformations, Lille, France, ³Geological Survey of Denmark and Greenland, Copenhagen, Denmark, ⁴Department of Geology and Geophysics, University of Utah, Salt Lake City, UT, USA, ⁵Laboratoire de Planétologie et Géodynamique, CNRS, UMR 6112, Université de Nantes, Nantes, France

Key Points:

- Geodynamic subduction model with experiment-informed mantle fabric transitions
- P -dependent olivine textures can explain the evolution of upper mantle anisotropy
- A relatively wet upper transition zone could likely explain faster V_{SH} than V_{SV} speeds

Supporting Information:

Supporting Information may be found in the online version of this article.

Correspondence to:

J. K. Magali and S. Merkel,
jkmagali@gmail.com;
sebastien.merkel@univ-lille.fr

Citation:

Magali, J. K., Thomas, C., Ledoux, E. E., Capdeville, Y., & Merkel, S. (2025). On the influence of pressure, phase transitions, and water on large-scale seismic anisotropy underneath a subduction zone. *Geochemistry, Geophysics, Geosystems*, 26, e2024GC011827. <https://doi.org/10.1029/2024GC011827>

Received 13 AUG 2024

Accepted 18 FEB 2025

Author Contributions:

Conceptualization: John Keith Magali, Christine Thomas, Sébastien Merkel

Formal analysis: John Keith Magali, Christine Thomas, Estelle Elisa Ledoux, Sébastien Merkel

Funding acquisition: Christine Thomas, Sébastien Merkel

Investigation: John Keith Magali

Methodology: John Keith Magali

Project administration: Christine Thomas, Sébastien Merkel

Resources: Estelle Elisa Ledoux, Yann Capdeville

© 2025 The Author(s). Geochemistry, Geophysics, Geosystems published by Wiley Periodicals LLC on behalf of American Geophysical Union.

This is an open access article under the terms of the [Creative Commons Attribution-NonCommercial-NoDerivs License](https://creativecommons.org/licenses/by/4.0/), which permits use and distribution in any medium, provided the original work is properly cited, the use is non-commercial and no modifications or adaptations are made.

Abstract Seismic anisotropy mainly originates from the crystallographic preferred orientation (CPO) of minerals deformed in the convective mantle flow. While fabric transitions have been previously observed in experiments, their influence on large-scale anisotropy is not well-documented. Here, we implement 2D geodynamic models of intra-oceanic subduction coupled with mantle fabric modeling to investigate the combined effect of pressure (P)- and water-dependent microscopic flow properties of upper mantle and upper transition zone (UTZ) minerals, respectively, on large-scale anisotropy. We then compare our anisotropy models with anisotropic tomography observations across the Honshu subduction zone. Our results for the upper mantle correlate well with observations, implying that the P -dependence of olivine fabrics is sufficient to explain the variability of anisotropy. Meanwhile, a dry UTZ tends to be near-isotropic whereas a relatively wet UTZ could produce up to 1% azimuthal and ~2% radial anisotropy. Because water facilitates CPO development, it is therefore likely a requirement to explain the presence of anisotropy in the transition zone close to subducting slabs.

Plain Language Summary Subduction causes the surrounding mantle to deform according to the movement and pressure exerted by the plates. This influences the alignment of minerals making up the mantle, which in turn, affects the speed and direction of seismic waves known as seismic anisotropy. In this study, we investigate the role of pressure in the upper mantle and water in the transition zone on large-scale seismic anisotropy across a subduction zone. In the upper mantle, we show that the patterns of anisotropy at places where deformation is presumed to be large are affected by changes in pressure. In the transition zone, anisotropy tends to favor a wetter environment.

1. Introduction

Understanding the dynamics of descending tectonic plates is crucial as it regulates, to first order, the coupling between deep mantle convection and surface deformation. For example, different styles of subduction that have been observed mark unique variations of mantle flow trajectories such as the promotion of rapid trench retreat in the case of stagnating slabs or strong changes in upper plate forcing in the case of slab penetration (e.g., Agrusta et al., 2017; Fukao & Obayashi, 2013). These distinct flow patterns which make up the convective mantle then facilitate the stretching and thinning of the sinking lithosphere and thus take part in the thermo-chemical evolution of the Earth's interior (Allègre & Turcotte, 1986). Changes in mineralogy and viscosity structure at designated mantle transition zone boundaries control the style of subduction, and to some extent, the overall dynamics of plate tectonics (Agrusta et al., 2017; Goes et al., 2017). A plethora of geophysical observables can be used to constrain mantle flow; one of them is seismic anisotropy.

Seismic anisotropy mainly results from the crystallographic preferred orientation (CPO) in intrinsically anisotropic minerals upon progressive deformation along convective flows (Long & Becker, 2010). The parameters ξ for S -wave radial anisotropy (i.e., the ratio of the squares of V_{SH} and V_{SV} for horizontally propagating S -waves) and a_z for azimuthal anisotropy (i.e., directional-dependence of V_{SV}) are simple yet intuitive ways of quantifying seismic anisotropy, and hence, are often constrained in tomographic imaging (e.g., Montagner, 1998; Panning & Romanowicz, 2006; Smith & Dahlen, 1973). In a subduction zone, anisotropic tomography suggests the mantle

Software: John Keith Magali, Yann Capdeville, Sébastien Merkel
Supervision: Sébastien Merkel
Writing – original draft: John Keith Magali
Writing – review & editing: John Keith Magali, Christine Thomas, Estelle Elisa Ledoux, Yann Capdeville, Sébastien Merkel

wedge is characterized by a layer of positive radial anisotropy $\xi > 1$ (e.g., Chang et al., 2015; French & Romanowicz, 2014; Simmons et al., 2021) and 2 – 3% peak-to-peak azimuthal anisotropy (e.g., Debayle et al., 2016; Yuan & Beghein, 2013). Underneath the oceanic lithosphere away from the slab, the patterns of anisotropy appear less complex exhibiting an age-independent distribution of $\xi > 1$ and $a_{V_{SV}}$ 2% with maximum amplitudes appearing at ~150 km (e.g., Chang et al., 2015; Debayle et al., 2016; Yuan & Beghein, 2013). Reduction of seismic anisotropy is observed past ~250 km depth (e.g., Burgos et al., 2014; Nettles & Dziewoński, 2008). Across the upper transition zone (UTZ, 410 – 520 km) around slabs, $\xi < 1$ and $a_{V_{SV}} \sim 1 - 2\%$ is generally observed (e.g., Montagner et al., 2021).

Subduction zones are hot beds for the development of complex seismic anisotropy patterns. The prevalent seismic anisotropy observed around them may be attributed either in terms of large strains that the entrained mantle adjacent to the slab experiences (Mainprice, 2007), structural layering of plate remnants (Karato, 1998), or possibly an interplay of both. In the upper mantle, the abundance of olivine primarily constitutes up to 18% variations in shear wave velocities (Kumazawa & Anderson, 1969). Thus, the observed large-scale anisotropy can mostly be attributed to the CPO of olivine aggregates deformed in the convective mantle (Long & Becker, 2010). Other factors such as the shape preferred orientation of partial melt across mantle wedges could also contribute to the overall anisotropy observed in the upper mantle (Vauchez & Garrido, 2001; Zimmerman et al., 1999). Laboratory simple shear experiments have revealed that the olivine fast axis tends to align itself with the direction of shear (S. Zhang & Karato, 1995). Often categorized as an A-type fabric, such is favored under low pressure and anhydrous conditions (Karato et al., 2008). With this, seismologists often interpret shear wave splitting patterns or the fast azimuth of Rayleigh wave phase velocities as the horizontal projection of flow in the upper mantle (e.g., Becker et al., 2003; Long & Silver, 2009). The rheology of olivine polycrystals, however, depend on several factors that may alter its plasticity behavior with respect to the imposed macroscopic deformation most notably temperature, pressure, and water content (Karato et al., 2008).

Veering from ~410 km, olivine undergoes pressure-induced phase transformation into wadsleyite which completely changes its plasticity behavior and its elastic properties (Ringwood, 1991). Assuming a pyrolytic mantle, where wadsleyite constitutes the majority of its total volume fraction, the intrinsic anisotropy of wadsleyite likely drives the development of the observed large-scale anisotropy in the UTZ, especially around subduction zones where vigorous straining are to be expected (e.g., Kawazoe et al., 2013). Aside from strain localization around slabs, the transport of water via subduction is reasonably efficient to hydrate the entrained mantle in the UTZ (Bercovici & Karato, 2003). Numerical simple shear experiments of wadsleyite suggest water promotes CPO development (Ledoux, Saki, et al., 2023; Zhou et al., 2022). Thus, it is also crucial to study the effect of water on large-scale anisotropy in the UTZ for complex flow fields.

A multidisciplinary approach involving geodynamic modeling with mineral physics constraints is required to understand the origin of large-scale anisotropy. Such methods have already been carried out in the previous decade (e.g., Faccenda, 2014; Sturgeon et al., 2019) with some even accounting for the effect of small-scale isotropic heterogeneities (Faccenda et al., 2019; Ferreira et al., 2019; Magali et al., 2021). Yet, the impact of fabric transitions onto large-scale seismic anisotropy which has been observed experimentally in mineral microstructures (e.g., Mainprice et al., 2005; Raterron et al., 2007), is not fully investigated for realistic flows, especially in a subduction setting where strains are large. While certain mantle conditions must be met to induce fabric transitions, we focus on the effect of pressure in the upper mantle and water in the UTZ based on previous findings that P -induced olivine slip transitions and water in the UTZ strongly influence the depth distribution of the observed radial anisotropy (Magali, Ledoux, et al., 2024). For simplicity, we will not consider the effect of water on upper mantle anisotropy.

Here, we build upon previous CPO modeling studies (e.g., Faccenda, 2014; Fraters & Billen, 2021; Li et al., 2014; Sturgeon et al., 2019) by integrating mantle fabric transitions to predict radial and azimuthal anisotropy underneath a subduction zone. We then apply elastic homogenization (Capdeville & Métivier, 2018; Capdeville et al., 2015) as a post-processing step, and compare the effective anisotropy with anisotropic tomography models across the Honshu arc. Two main problems will be addressed using our modeling strategy: (a) Determine whether P -induced slip transitions in olivine could sufficiently explain the variability of anisotropy in the upper mantle, and (b) investigate the role of water in the development of anisotropy in the UTZ using the recently published texture data of wadsleyite (Ledoux, Saki, et al., 2023; Ohuchi et al., 2014).

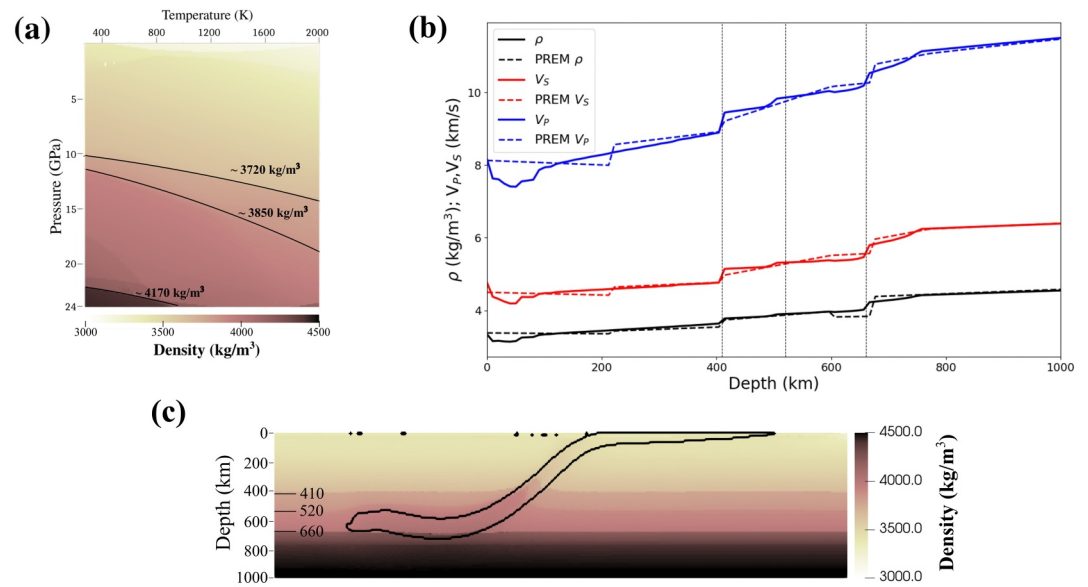


Figure 1. (a) Density map predicted from *Perple_X* for a pyrolitic mantle composition. Black contour lines correspond to arbitrary density crossovers associated with the following phase transitions: Olivine → wadsleyite ($\rho_{410} = 3,720 \text{ kg} \cdot \text{m}^{-3}$), wadsleyite → ringwoodite ($\rho_{520} = 3,850 \text{ kg} \cdot \text{m}^{-3}$), and ringwoodite → bridgmanite ($\rho_{660} = 4,170 \text{ kg} \cdot \text{m}^{-3}$). (b) Predicted 1D density, V_P and V_S structure of pyrolite (solid lines) versus the preliminary reference Earth model, PREM (Dziewonski & Anderson, 1981) (dashed lines). (c) Density structure of our subduction model at the present time using (a). Solid black lines delineate the subducting slab.

2. Methods

2.1. Geodynamic Modeling of Intraoceanic Subduction

We carry out 2D $6000 \text{ km} \times 1000 \text{ km}$ thermo-chemical modeling of intraoceanic subduction with viscoplastic rheology using the open software ASPECT (Kronbichler et al., 2012) which solves the conservation of mass, momentum, and energy equations for an incompressible fluid. Initial temperature of the oceanic and overriding plates follow an age-base plate-cooling model that increases toward the trench (Schubert et al., 2001) (Figure S1a in Supporting Information S1). The governing equations are coupled with an advection equation for four compositional fields: subducting plate, overriding plate, subducting crust, and background mantle, each of which possesses distinct rheological properties (Glerum et al., 2018). The transition zone is characterized by phase transitions that may either inhibit or assist subduction: olivine to wadsleyite at $\sim 410 \text{ km}$, wadsleyite to ringwoodite at $\sim 520 \text{ km}$ and finally ringwoodite to bridgmanite at $\sim 660 \text{ km}$. As we are only interested in upper mantle and UTZ anisotropy, we limit our modeling to a slab stagnating at 660 km . Full details in its implementation, including the values of some parameters describing a viscoplastic rheology and phase transition information can be found in Text S1 and Tables S1 and S2 in Supporting Information S1.

Pressure-induced phase transformations vary the textural properties of a material crossing a phase transition boundary, and as a consequence, produce distinct patterns of large-scale seismic anisotropy at certain depths. To constrain the boundaries, we employ *Perple_X* (Connolly, 2005, 2009) to retrieve an equilibrium mineral assemblage for a given temperature T , pressure P , and bulk composition. We use the recently published thermodynamic database of Stixrude and Lithgow-Bertelloni (2022) to estimate the density ρ as a function of P and T assuming a pyrolitic mantle (Figure 1a) which we also benchmarked against the preliminary reference Earth model of Dziewonski and Anderson (1981) (Figure 1b). Figure 1c shows the predicted ρ of the subduction model and the associated crossovers ($\rho_{410} = 3720 \text{ kg} \cdot \text{m}^{-3}$, $\rho_{520} = 3850 \text{ kg} \cdot \text{m}^{-3}$, $\rho_{660} = 4170 \text{ kg} \cdot \text{m}^{-3}$; where subscripts indicate phase transition depths).

2.2. Mantle Fabric Modeling

As a post-processing step, ASPECT saves each pressure P , temperature T , and velocity \mathbf{u} fields corresponding to different time steps in an unstructured grid format. To account for time-dependent deformation when tracing

pathlines, we estimate the local velocity gradient L' , local total pressure (hydrostatic + dynamic) P' , and local temperature T' by interpolating new P , T , and \mathbf{u} fields each time at a point along the pathline. Local density ρ' along the pathline is estimated at the given P' and T' with the help of the density map shown in Figure 1a. Note that the primed variables indicate the values of the physical parameters computed along the pathline. At the final time step t_{final} , tracers are regularly distributed above the 660-km boundary shown in Figure 1c where anisotropy would be calculated. We use the full L' for strain accumulation.

To model mantle fabrics, we implement the modified viscoplastic self-consistent (VPSC) method of Lebensohn and Tomé (1993) that incorporates P -induced olivine a- to c-slip transition, with [100](010) dominant slip at low P and [001](010) dominant slip at high P (Raterron et al., 2014), and P -induced phase transformations as implemented in Magali, Ledoux, et al. (2024). While kinematic models are less computationally demanding and can replicate large-scale anisotropy features (e.g., Kaminski et al., 2004), VPSC offers the capability to work with an arbitrary number of independent slip systems. Furthermore, it explicitly accounts for variations in intragranular stress and strain, resulting in more precise predictions of the mechanical behavior of deforming polycrystals (Castelnau et al., 2008). Each tracer with density ρ' is composed of 3,000 initial randomly oriented grains with the following modal abundancies: Upper mantle ($\rho' < \rho_{410}$): 60% P -dependent olivine (Magali, Ledoux, et al., 2024) and 40% other phases (assumed isotropic), UTZ ($\rho_{410} \leq \rho' < \rho_{520}$): 60% wadsleyite (Ledoux, Saki, et al., 2023) and 40% garnet, and lower transition zone (LTZ, $\rho_{520} \leq \rho' < \rho_{660}$): 60% ringwoodite and 40% garnet. Both garnet and ringwoodite are deemed isotropic (e.g., Mainprice, 2007). The single crystal elastic constants of the phases at ambient conditions, including their PT derivatives are listed in Table S3 in Supporting Information S1. Wadsleyite properties are more complex to incorporate and will henceforth be discussed below.

2.3. An Ersatz to Compute Water-Dependent Anisotropy in the Transition Zone

In this study, we assume that the ambient UTZ is dry and the slab, together with the entrained mantle, is relatively wet. To do this, tracers are specified with either hydrous (i.e., C_{wd} -type) or dry wadsleyite (i.e., B_{wd} -type) depending on their positioning relative to the slab (Ledoux, Saki, et al., 2023). VPSC simulations of B_{wd} -type and C_{wd} -type wadsleyite deformed under simple shear are shown in Figure S2 in Supporting Information S1. Tracers with $T' < 1750$ K envelope the cold and slightly hydrated slab, and hence C_{wd} -type CPO is calculated. Consequently, those with $T' \geq 1750$ K are prescribed with a B_{wd} -type fabric. The latter corresponds to tracers scattered around the dry and ambient UTZ. We also test the effect of a fully dry UTZ by computing the CPO of B_{wd} -type wadsleyite aggregates across the entire UTZ.

P and T -dependent wadsleyite polycrystal elastic tensors are also computed using Voigt-Reuss-Hill averaging around their single crystal counterparts. Hydrous and dry elastic constants are inferred from Zhou et al. (2022) and Núñez-Valdez et al. (2013), respectively (Table S3 in Supporting Information S1). CPO of a tracer crossing a phase transition boundary determined by the density crossovers is erased and instead replaced with random textures according to experimental results of microstructures induced by the olivine \rightarrow wadsleyite transition (Ledoux, Krug, et al., 2023; Smyth et al., 2012). Anisotropy calculations are ceased past $\rho' = \rho_{660}$. Mineral assignments are summarized in Figure 2a.

2.4. Elastic Homogenization

For a realistic comparison with anisotropic tomography models, we first apply the fast-Fourier homogenization (FFH) algorithm to obtain an effective medium void of spatial heterogeneities whose scales are much smaller than the minimum wavelength λ_0 of the observed wavefield used in seismic tomography. The foundation behind this method is detailed in Capdeville et al. (2010, 2015), and its application to anisotropic media is described in Magali et al. (2021) and Magali, Ledoux, et al. (2024a). The effective medium is a smooth tomographic version of the true medium, similar to an image recovered by full waveform inversion assuming perfect data coverage (Capdeville & Métivier, 2018). Once the effective medium is obtained, we apply the elastic decomposition method of Montagner and Nataf (1986) to compute radial anisotropy ξ and peak-to-peak azimuthal anisotropy strength a_z (Texts S2 and S3 in Supporting Information S1).

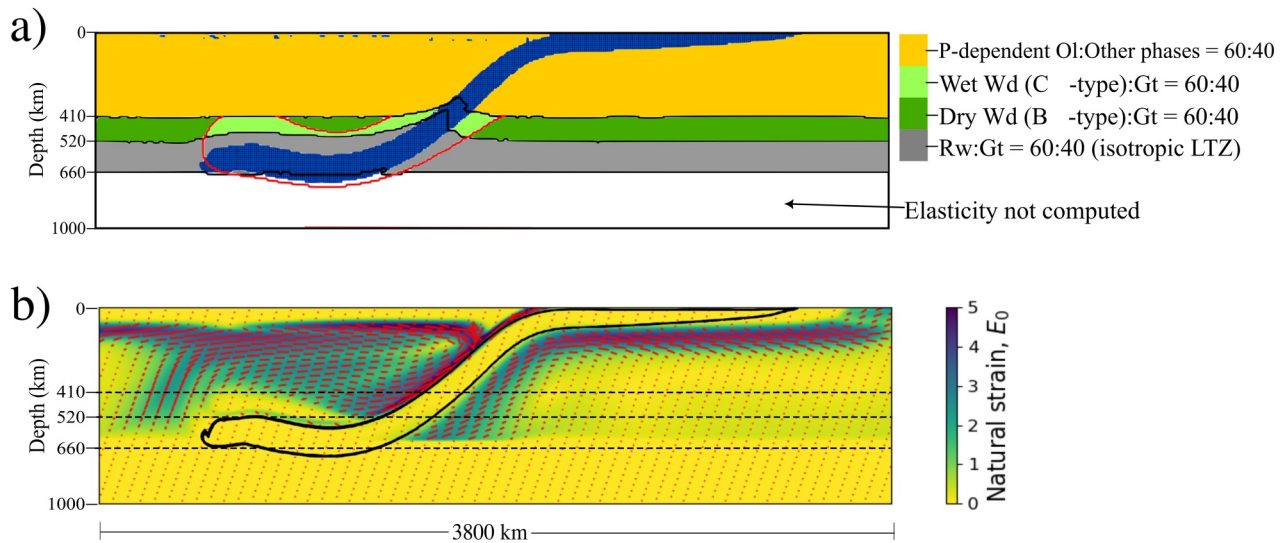


Figure 2. (a) Distribution of mineralogical fabrics across the subduction zone at the present day: Ol—olivine, Wd—wadsleyite, Gt—garnet, Rw—ringwoodite. In the upper transition zone, the distribution of hydrous and dry Wd is solely determined by the evolution of the 1,750 K isotherm (solid red line) that encapsulates the slab (in blue). Solid black lines are the predicted topographies of the phase transition boundaries. For a fully dry UTZ, dark green shades associated with C_{wd} -type wadsleyite cover the entire UTZ. (b) Amount of accumulate strain, called natural strain E_0 . Arrowless vectors correspond to the finite strain ellipse major semi-axis.

3. Results

3.1. Textures at Selected Zones Across the Subduction Zone

We select several zones along independent pathlines where strains are presumed to be large to examine the orientations of the crystallographic axes in the evolved CPO of P -dependent olivine aggregates in the upper mantle (i.e., Figures 3a–3g) and C_{wd} -type wadsleyite aggregates within the hydrous region of the UTZ (Figures 3h–3j). Across the mantle wedge, zone *a* exhibits relatively weak CPO with [100] oriented sub-parallel to the vertical z direction. Moving closer to the slab, large deformation gradients lead to stronger textures oriented sub-parallel to the flow direction in zones *b* and *c*. At zone *d*, rapid trench retreat results in relatively strong [010] orientations. Across the subslab mantle, we see clusters of the [100] axes becoming thicker around the y direction starting from zone *g* to *e*. Increased activities at the [001](010) slip systems with depth lead to weaker overall textures from zone *g* to *e*. Across the upper transition zone, locations *h* – *j* represented by C_{wd} -type wadsleyite fabrics (i.e., hydrous) exhibit dominant activity at $\langle 111 \rangle \{101\}$ that induces CPO with oblique [100] and [001] axes relative to the flow direction.

3.2. Predictions of Large-Scale Upper Mantle Anisotropy Induced by Subduction

As implemented in current literature (e.g., Faccenda, 2014; Ferreira et al., 2019; Li et al., 2014; Sturgeon et al., 2019) and for the sake of comparison, we also compute upper mantle anisotropy based on an A-type olivine fabric. When upscaled to upper mantle conditions, A-type olivine appears to overestimate the overall strength of radial (Figures 4c and 4d) and azimuthal anisotropy (Figures 5c and 5d), measuring up to $\xi \sim 1.14$ and $a_z \sim 12\%$ across the upper 250-km of the subplate mantle. Akin to Magali, Ledoux, et al. (2024), incorporating P -induced slip transitions in olivine in a geodynamic model tones down the overall strength of anisotropy in the same region to $\xi \sim 1.08$ (Figures 5a and 5b) and $a_z \sim 5\%$ (Figures 5a and 5b). The influence of the latter can also be observed across the subslab mantle (zones *g* – *e* in Figure 3) where anisotropy strength decreases rapidly with depth; dropping to $\xi \sim 1.01$ and $a_z \sim 1\%$ at $z = 400$ km. Meanwhile, the A-type case still retains up to $\xi \sim 1.06$ and $a_z \sim 8\%$ at $z = 400$ km. Since the amount of accumulated strain appears to be maintained down to 410 km in the subslab mantle (Figure 2b), the presumed switch in primary activities from the [100](010) to the [001](010) slip systems may have caused this reduction of anisotropy with depth (Magali, Ledoux, et al., 2024; Raterron et al., 2014).

The mantle wedge also mostly exhibits an overestimated amount of positive radial anisotropy $\xi > 1$ (Figure 4b) and azimuthal anisotropy (Figure 5b) in the A-type case that spans down to the 410-km phase transition boundary.

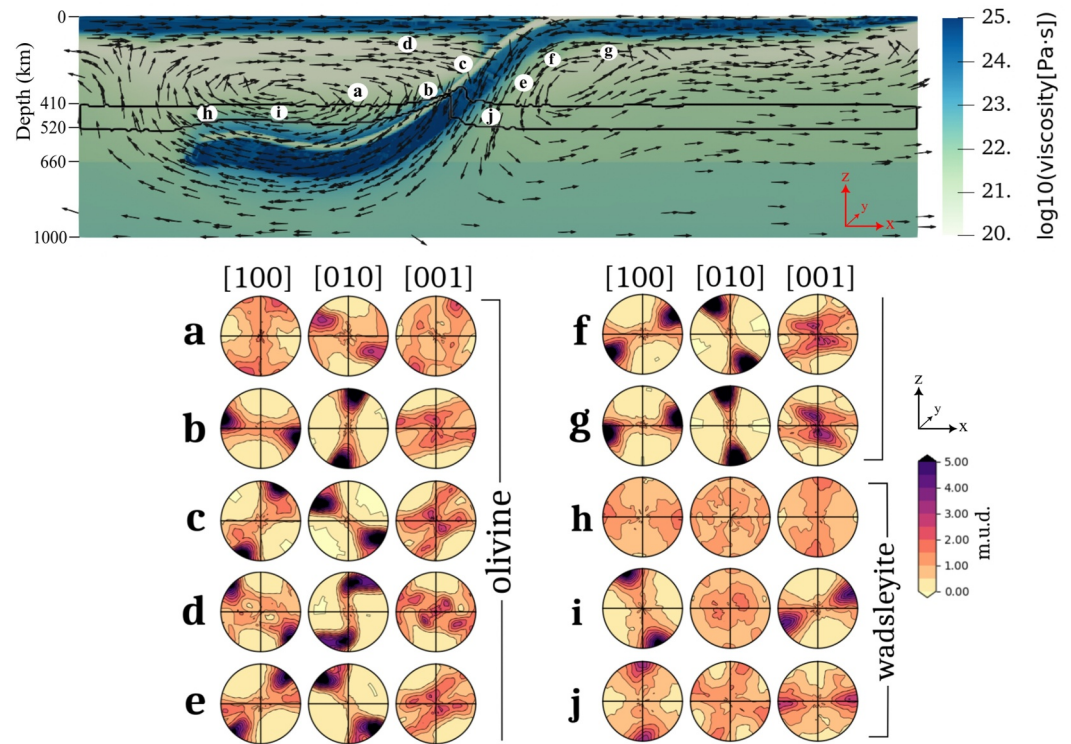


Figure 3. Top panel: Effective mantle viscosity at the present day in $\log[\text{Pa}\cdot\text{s}]$ units. Dark solid lines delineate the presumed topography of the 410 and 520-km seismic discontinuities assuming a pyrolitic mantle. Arrows represent mantle flow velocity. Bottom panel: Computed textures at selected zones along the model, *a-g* for *P*-dependent olivine and *h-j* for hydrous wadsleyite, respectively. M.u.d. refers to the multiples of uniform distribution which measures texture strength.

In the *P*-dependent case (Figure 4a), the entrained mantle immediately beneath the back-arc basin (zone *d* in Figure 3) experiences rapid trench retreat motion due to a decreased upper plate forcing of a thin overriding lithosphere (Agrusta et al., 2017). This creates a localized region of negative radial anisotropy $\xi < 1$. Meanwhile, $\xi \sim 0.97$ and near-zero azimuthal anisotropy are generated just above the UTZ close to the slab (zone *a* in Figure 3). Comparison with the finite strain ellipse (FSE) at depths comparable to zone *a* indicates that the anisotropy fast axis resulting from *P*-dependent fabrics (Figures 4a and 4b) appear nearly normal to the sub-horizontal FSE long axis orientation (Figure 2b). Li et al. (2014) revealed aggregates submitted to subduction zone stresses exhibit olivine [100] axes that are approximately aligned with the FSE long axis in the case of an A-type fabric. This translates to large-scale patterns that appear positively radial anisotropic $\xi > 1$ along zone *a* (Figures 4c and 4d). The existence of a negative radial anisotropy $\xi < 1$ at these depths in the *P*-dependent case and the absence of these localized $\xi < 1$ features in the mantle wedge in the A-type case both suggest that the *P*-dependent model is more consistent with observations.

3.3. Effect of Water Around the Slab on Mantle Transition Zone Anisotropy

A wet UTZ near the slab is generally characterized by an accumulation of negative radial anisotropy with $\xi \sim 0.97$ above the slab (zone *i* in Figure 3) and $\xi \sim 0.98$ in the slab area (zone *j*) (Figure 4a). A localized area of weak positive radial anisotropy ($\xi \sim 1.01$) forms close to the slab tip which can be attributed to the preferential alignment of the [100] axes of the C_{wd} -type phase with the horizontal (Figure 3 zone *h*) in response to rapid changes in the deformation patterns of the entrained mantle close to the slab tip. Small amounts of azimuthal anisotropy $a_z \sim 1.1\%$ far from the slab tip and up to $a_z \sim 1\%$ in the remaining regions close to the slab can be found (Figure 5a).

Figures 4b and 5b show the results of the same calculations assuming a fully dry transition zone (i.e., B_{wd} -type texture and elastic constants retrieved from Núñez-Valdez et al. (2013)). Such an assumption leads to an almost

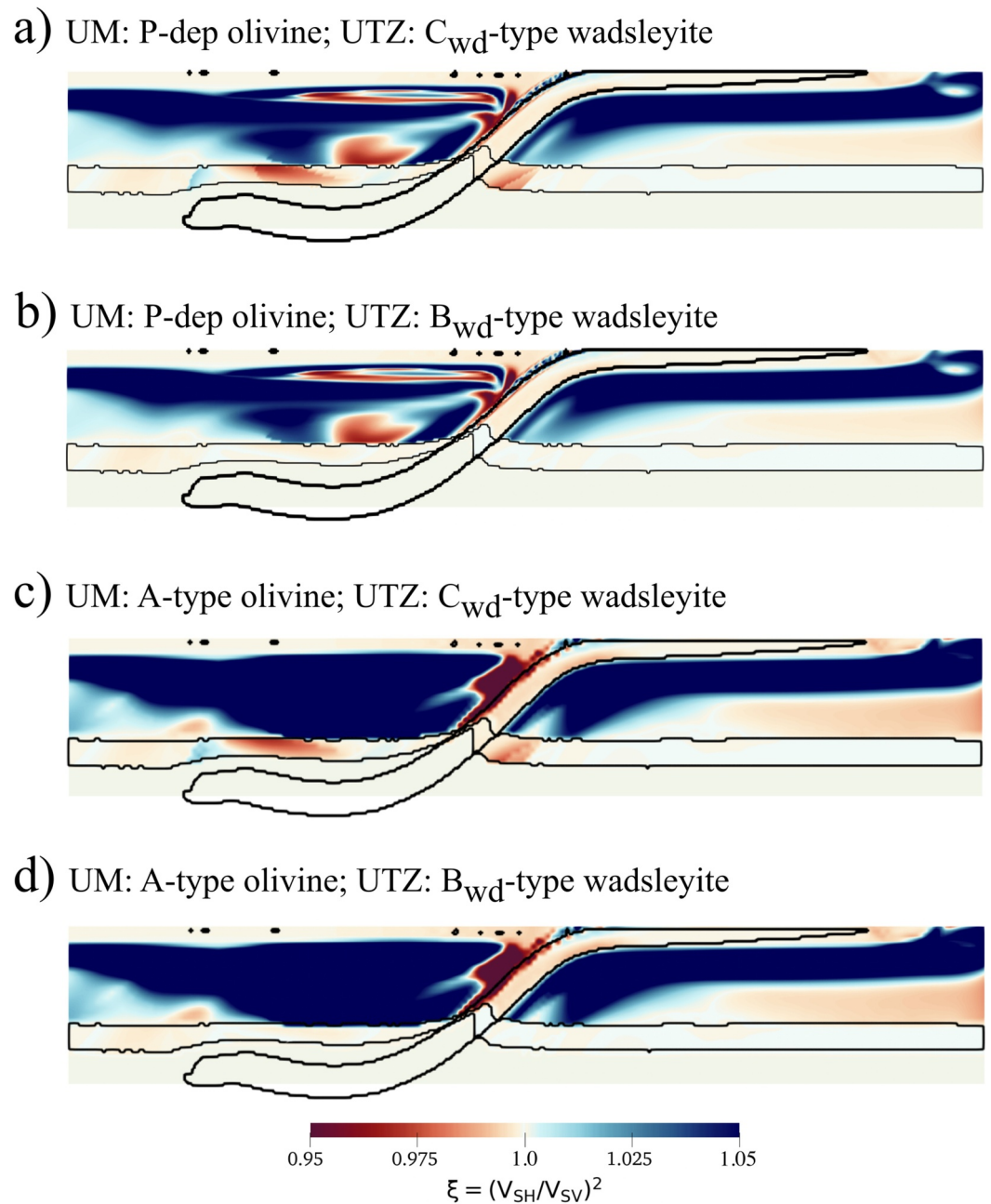


Figure 4. (a) Radial anisotropy parameter $\xi = (V_{SH}/V_{SV})^2$ for an upper mantle (UM) consisting of 60% *P*-dependent olivine aggregates and an upper transition zone (UTZ) with 60% C_{wd}-type wadsleyite (i.e., a wet UTZ). (b) Same as (a) but for a UTZ consisting of B_{wd}-type wadsleyite (i.e., a dry UTZ). (c) Same as (a) but for a UM model consisting of A-type olivine. (d) Same as (c) but for a dry UTZ.

isotropic UTZ around the slab. $a_z \sim 1.1\%$ away from the slab tip can also be detected which means that dry fabrics can produce enough azimuthal anisotropy but may fail to generate observable radial anisotropy.

3.4. Comparison With Tomographic Observations: A Case for the Honshu Arc

We select cross-sections of radial anisotropy and azimuthal anisotropy from SGLOBE-Rani (Chang et al., 2015) and 3DLGL-TPESv.v2022-11 (Debayle et al., 2016), respectively, in the Honshu subduction zone which displays, to some extent, a similar subduction style to our model. As part of the series of stagnant subduction systems

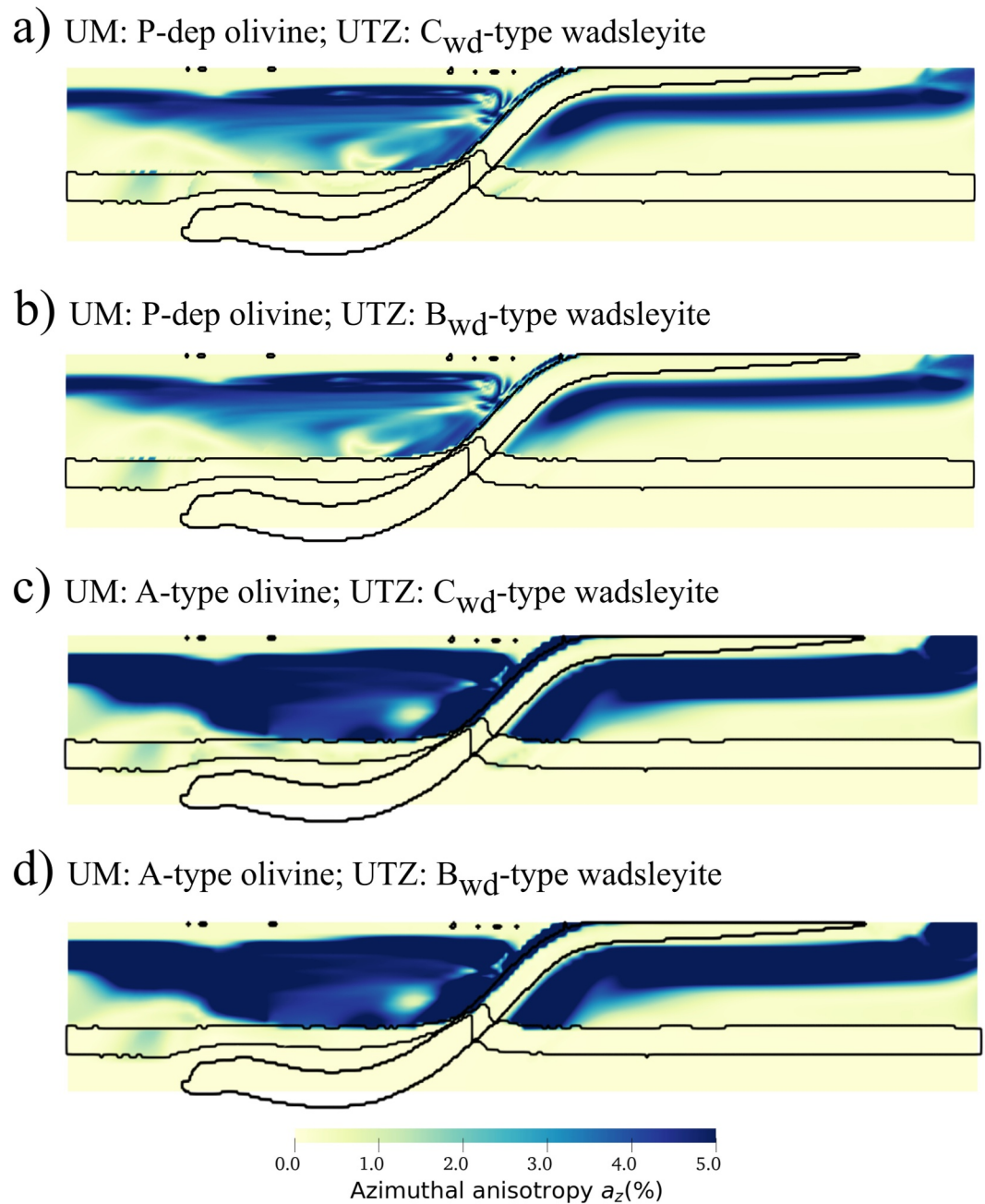


Figure 5. (a) Peak-to-peak azimuthal anisotropy a_z for an upper mantle (UM) consisting of 60% P -dependent olivine aggregates and an upper transition zone (UTZ) with 60% C_{wd} -type wadsleyite (i.e., a wet UTZ). (b) Same as (a) but for a UTZ consisting of B_{wd} -type wadsleyite (i.e., a dry UTZ). (c) Same as (a) but for a UM model consisting of A-type olivine. (d) Same as (c) but for a dry UTZ.

that span the Izu-Bonin and Japan regions, the Honshu arc is extensively studied owing to its ongoing tectonic processes (Wakita, 2018) and the broad distribution of receivers deployed in the area (Nanjo et al., 2010). The recent thermal and tectonic evolution of Honshu has likely been primarily influenced by the opening of the Japan Sea, which occurred around 14–28 million years ago (Sato et al., 2004). This led to its current slab morphology that appears to be flat, and dipping at $\sim 30^\circ$ (Honda & Yoshida, 2005). Notwithstanding the simplicity of the subduction process, cumulative deformation below the slab at UTZ depths is sufficient to produce noticeable shear wave splitting patterns (Figure 6: Left panel) with delay times of about ~ 1 and 2 s (Nowacki et al., 2015). While our models predict negligible V_S anisotropy for a dry UTZ, a wet UTZ composed solely of hydrous

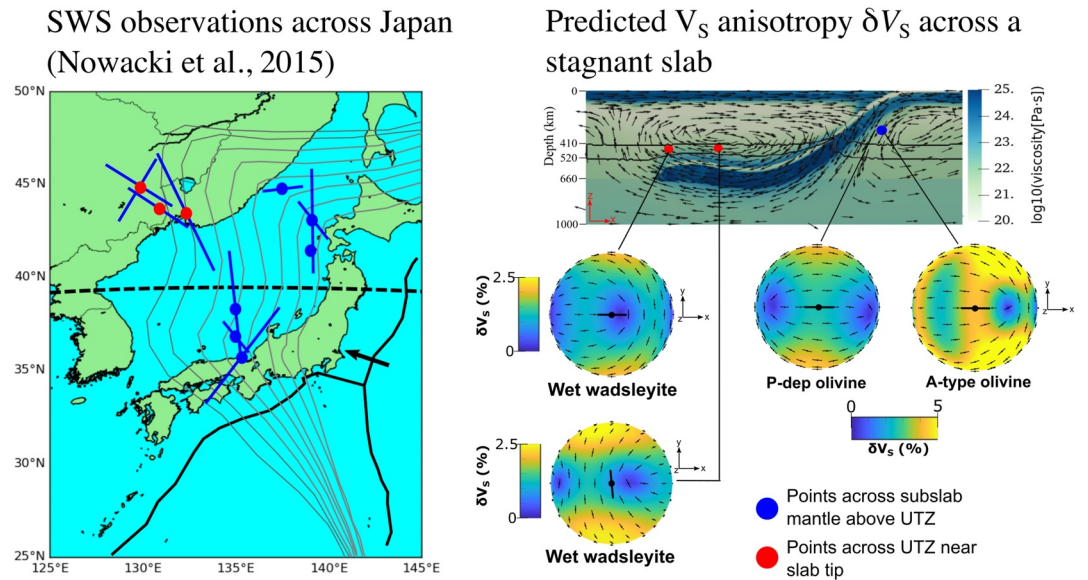


Figure 6. Left panel: Source-side shear wave splitting (SWS) observations across the Japan arc retrieved from Nowacki et al. (2015). Solid blue lines correspond to fast polarization directions. Dashed dark line best represents a cross section of the Honshu arc. Right panel: Predicted S-wave anisotropy δV_S at selected zones from our stagnant slab model. δV_S for dry wadsleyite (i.e., B_{wd} -type fabric) fabric is not included as B_{wd} -type fabrics produce negligible V_S anisotropy $\delta V_S \sim 0.1\%$. In both panels, blue circles correspond to points above the UTZ across the subslab mantle while red circles are to that of points below the UTZ near the slab tip.

wadsleyite could potentially explain both trench-parallel and trench-perpendicular observations (Figure 6: Right panel). Meanwhile, neither P -dependent nor A-type olivine could explain the along-strike observations. This either warrants toroidal flows produced from 3D convection models (Faccenda & Capitanio, 2012, 2013; Pirmallo et al., 2006) or the incorporation of olivine rheology inferred from empirical laws of hydrous exponential creep if limited to 2D flows (Katayama & ichiro Karato, 2006; Kneller et al., 2007).

Homogenization is performed only in CPO models with a P -dependent upper mantle anisotropy coupled with a wet UTZ since A-type olivine fabric tends to overestimate upper mantle anisotropy and that no substantial anisotropy is developed assuming a fully dry UTZ. To date, SGlobe-Rani (Chang et al., 2015) and 3DLGL-TPESv.v2022-11 (Debaille et al., 2016) are two of the most comprehensive global anisotropy models with the former having over 100,000 free-surface reflected S waves as data that help constrain upper mantle and transition zone structures, and the latter having over 2,000,000 Rayleigh wave observations up to the fifth overtone to constrain azimuthal anisotropy at upper and mid-mantle depths. We consider homogenization wavelengths of $\lambda_0 = 65$ km and $\lambda_0 = 164$ km for ξ and a_z , respectively. For comparisons of ξ with SGlobe-Rani, the chosen value of λ_0 is a conservative estimate of the wavelength of SS phases with dominant periods of roughly 10 – 15 s used to sample the upper mantle and the UTZ when conducting the inversion (Chang et al., 2015). For comparisons of a_z with 3DLGL-TPESv.v2022-11, this roughly corresponds to the minimum period ~ 40 s of first overtones used in the inversion with maximum sensitivity kernels at the same depth range (Debaille et al., 2016). It is noteworthy that actual comparisons with these tomography images may warrant the convolution of our anisotropy models with their resolution filters to account for incomplete data coverage (Kendall et al., 2022; Simmons et al., 2019). While this could be a subject of future work, addressing finite frequency effects through homogenization is sufficient for the time being to correlate our anisotropy models with observations (Magali et al., 2021).

Figures S3 and S4 in Supporting Information S1 show the effective anisotropy models at different homogenization wavelengths λ_0 . Here, small-scale anisotropic features lose their identity with increasing λ_0 due to the increasing degree of spatial averaging.

3.4.1. Effective Radial Anisotropy ($\lambda_0 = 65$ km) Comparison With SGLOBE-Rani

Localized areas of the observed negative radial anisotropy $\xi_{\text{obs}} < 1$ underneath the back-arc basin and just above the stagnant slab is evident (Figure 7b). Whether these peculiar features are robust or not, however, warrants

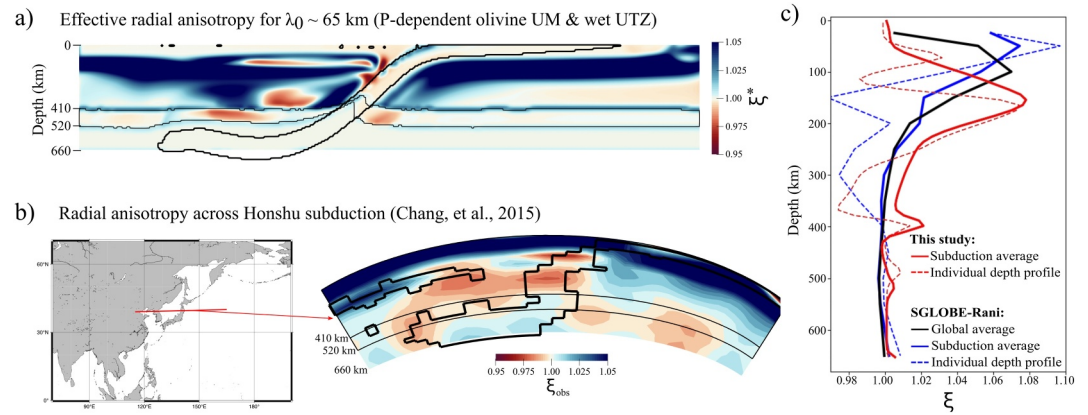


Figure 7. (a) Effective radial anisotropy ξ^* at $\lambda_0 = 65$ km for a P -dependent upper mantle (UM) and a wet upper transition zone (UTZ) model. (b) Radial anisotropic tomography image across the Honshu arc retrieved from SGlobe-Rani (Chang et al., 2015). Dark contours indicate $+0.5\%$ isotropic V_S anomalies that delineate the presumed slab retrieved from 3DLGL-TPESv.v2022-11. (c) 1D radial anisotropy profiles from our model (in red), across Honshu (in blue), and global average (in black). At each depth, global average is obtained by taking the mean of ξ in both the latitude (lat) and longitude (lon), whereas subduction average is obtained by taking the mean of ξ along a cross section defined by the following starting and ending coordinates [lat, lon]: $[36^\circ, 105^\circ], [37^\circ, 170^\circ]$. Individual depth profiles are constructed by simply selecting the value of ξ at given depth below the presumed back-arc basin. The choice of λ_0 is a conservative estimate for the wavelength of the SS phase sampling the upper mantle and the UTZ.

regional tomography for better resolution. Nonetheless, their presence can be reproduced with a geodynamic model that accounts for transient flows and P -dependent fabrics in olivine (Figure 7a). In the UTZ, modeling with wet wadsleyite fabrics captures the persistence of $\xi_{\text{obs}} < 1$ near the slab. P -induced phase transformations from olivine to wadsleyite at ~ 410 km, and to ringwoodite at ~ 520 km introduce sharp velocity contrasts that when homogenized, produce a thin layer of weak $\xi^* > 1$ which is not observed in SGlobe-Rani. Finally, ξ^* cannot explain the prevalence of ξ_{obs} in the LTZ. Small-scale heterogeneities unaccounted for in our model such as petrological layering of transformed subducted material could explain such observations (Karato, 1998). Smearing effects from the tomographic inversion could also lead to the presence of radial anisotropy in the LTZ.

3.4.2. Effective Azimuthal Anisotropy ($\lambda_0 = 164$ km) Comparison With 3DLGL-TPESv.v2022-11

Choosing a longer homogenization wavelength ($\lambda_0 \sim 165$ km) intensifies the spatial averaging of small-scale heterogeneities in azimuthal anisotropy (Figure 8a). This leads to a decrease in azimuthal anisotropy of about 1%. Comparison with the 3DLGL-TPESv.v2022-11 tomographic model (Figure 8b) is not as robust as with our result from ξ^* with SGlobe-Rani. For instance, the consistent azimuthal anisotropy at depths above ~ 250 km predicted from our model only appears in patches in 3DLGL-TPESv.v2022-11. Furthermore, the predicted anisotropy in the UTZ is significantly underestimated (Figure 8c). Several factors may be involved in the difference between a_z^* and a_z^{obs} . The first may be related to ad-hoc constraints on regularization where the spatial distribution of a_z^{obs} is bounded to this uncertainty. Another factor relates to the dimensionality of our model. Here, although the elastic tensors computed from VPSC are in 3D, the latter relies on a 2D representation of thermochemical subduction. Thus, toroidal flow was not taken into account which was shown to participate in the production of trench-parallel anisotropy (Faccenda & Capitanio, 2012, 2013; Li et al., 2014), and hence a rather complex distribution of azimuthal anisotropy (e.g., Rychert et al., 2012).

4. Discussion

4.1. Pressure-Dependence of Single-Phase Fabrics and Its Implications for the Upper Mantle

Laboratory studies have already reported the existence of pressure-dependence of olivine microstructures (Jung et al., 2009; Mainprice et al., 2005; Ohuchi et al., 2011; Raterron et al., 2007), and most recently of bridgmanite (Gay et al., 2024). To this day, however, it is still not clear how textures evolve with hydrostatic pressure (Karato et al., 2008) since high- P experiments are also characterized by high differential stresses $\sigma \sim 100 - 500$ MPa which could contribute to fabric transitions (e.g., Katayama et al., 2004). Deformed peridotites extracted from

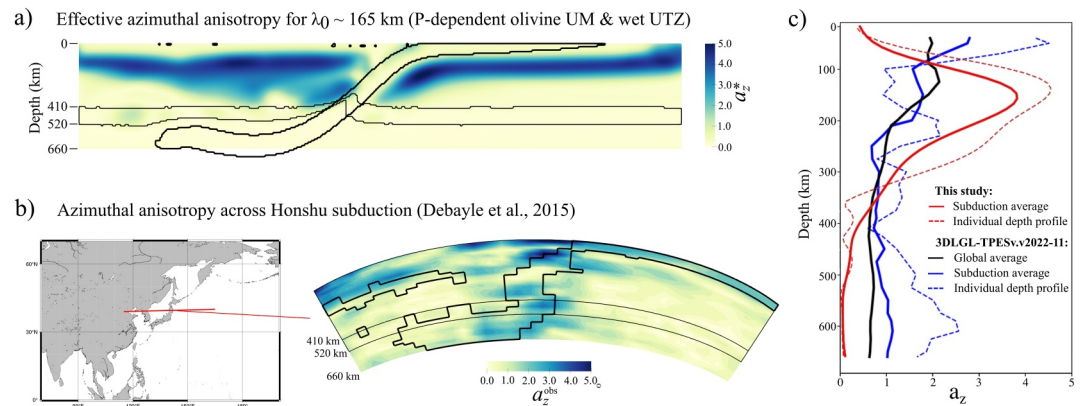


Figure 8. (a) Effective azimuthal anisotropy after homogenization a_z^* at $\lambda_0 = 165$ km for a P -dependent upper mantle (UM) and a wet upper transition zone (UTZ) model. (b) Azimuthal anisotropic tomography image across the Honshu arc retrieved from 3DLGL-TPESv.v2022-11 (Debayle et al., 2016). Dark contours indicate +0.5% isotropic V_S anomalies that delineate the presumed slab taken from 3DLGL-TPESv.v2022-11. (c) 1D azimuthal anisotropy profiles from our model (in red), across Honshu (in blue), and global average (in black). At each depth, global average is obtained by taking the mean of ξ in both the latitude (lat) and longitude (lon), whereas subduction average is obtained by taking the mean of ξ along a cross section defined by the following starting and ending coordinates [lat, lon]: [36°, 105°], [37°, 170°]. Individual depth profiles are constructed by simply selecting the value of a_{zi} at given depth below the presumed back-arc basin. The chosen value of λ_0 roughly corresponds to the wavelength of first overtones with maximum sensitivity kernels at that same depth range.

xenoliths gathered mostly from the Western US, however, recorded lower differential stresses of about ~ 30 MPa (Bernard et al., 2019). Under low σ , Raterron et al. (2012) numerically demonstrated using the first-principles approach of Durinck et al. (2007) the slip transition from [100](010) to [001](010) olivine slip system in the deep upper mantle; consistent with Raterron et al. (2007), Jung et al. (2009), and Ohuchi et al. (2011).

4.1.1. Can P -Induced Slip Transitions Be Used as a Proxy to Describe the Alphabet Fabrics (i.e., A-, B-, C-, and E-Type Olivine)?

The response of strain-induced anisotropy on pressure becomes more evident in regions associated with large deformation (Magali, Ledoux, et al., 2024); in our model, across the mantle wedge and the slab mantle where the entrained mantle experiences first-hand the influence of slab pull. At low pressures, our implementation of P -induced olivine fabric transitions emulates an A-type fabric because of increased activities at the [100](010) slip system as shown by the alignment of the [100] axes with the direction of flow in zones *c* and *f-g* in Figure 3. At high pressures, it somehow follows a B-type fabric due to the switch in primary activities to the [001](010) slip system, for example, as evidenced by the slow rotation of the [100] textures toward the *y* direction at zone *e* in Figure 3 (Raterron et al., 2012, 2014). While P -induced apparent B-type fabrics could explain the distribution of anisotropy around the slab at high pressures, we could also not dismiss the effect of water on the generation of such fabric at low confining pressures (Ohuchi et al., 2012). Proxies of a water-rich environment in the convective flow are required to differentiate the possible origin (i.e., P -induced or water-induced) of B-type fabrics; although there is still no apparent relationship between olivine fabric types and water fugacity (Bernard et al., 2019).

Different conditions must be met to derive a suite of fabrics other than A- and B-type. Under low stresses and at increasing temperatures and a relatively dry mantle, an A-type transitions to an E-type (easiest slip system at [100](001)) fabric, and increasing water content, to a C-type (easiest slip system at [001](100)) fabric (Karato et al., 2008). Results from geodynamic simulations of upper mantle flow suggest $\xi > 1$ for A, B, and E-type fabrics, with E-type exhibiting minimal strength, whereas $\xi < 1$ for C-type, in the case of horizontal simple shear. As for a_z , all except B-type exhibit fast propagation directions parallel to the direction of shear (Long & Becker, 2010).

While it is tempting to infer the potential distribution of such fabrics across a subduction zone based on the distribution of ξ and a_z , doing so requires an extension of a depth-dependent model for anisotropy. Therefore, P -dependent olivine cannot be used as a proxy to describe fabric types. Lateral dependence can be accomplished

by tracking the effect of temperature and differential stresses on olivine slip systems critically resolved shear stresses (CRSS), for example, using first-principle calculations coupled with the Peierls–Nabarro formalism for olivine plasticity (e.g., Durinck et al., 2007). Nevertheless, we anticipate that classifying fabrics using large-scale anisotropy models alone would be difficult to execute. For better classification, textures derived from old fabrics must be completely overwritten by newer textures developed from a set of CRSS that reflect the current fabric.

4.1.2. On the Reduction of Free-Parameters to Constrain Patterns of Large-Scale Anisotropy

In recent years, models of upper mantle anisotropy are derived from carefully chosen methodologies such as: (a) implementation of a two-phase aggregate composed of 60% olivine and 40% enstatite reminiscent of a pyrolytic mantle (Ringwood, 1991), (b) strain partitioning where a fraction accommodated by dislocation creep is used for CPO development consistent with Karato and Wu (1993), and (c) the extension of homogenization methods for CPO modeling by incorporating dynamic recrystallization. Several studies have applied such methodologies in a subduction setting while assuming an A-type olivine fabric (e.g., Faccenda, 2014; Faccenda & Capitanio, 2012; Ferreira et al., 2019; Sturgeon et al., 2019). Here, the variability of ξ has been decently predicted in places where positive radial anisotropy $\xi > 1$ is ubiquitous such as the subplate mantle. Implementation of such methodologies, however, becomes increasingly difficult due to the sheer amount of free parameters that control the variability of anisotropy. This is not to say that these methods should be neglected given that such values can be obtained from literature. However, a more grounded approach should not be ruled out either. We argue that a simple depth-dependent anisotropy of single-phase aggregates, without the need for strain partitioning and additional mechanisms for CPO development, is enough to explain the variability of large-scale anisotropy in the upper mantle. This is especially true given the uncertainty surrounding where dislocation creep should subjugate (Becker & Lebedev, 2021; Hirth & Kohlstedt, 2003) and the inability of seismic waves to distinguish deformation from recrystallization textures (Wenk & Tomé, 1999).

4.2. Importance of Water on the Variability of Transition Zone Anisotropy

In light of our conducted numerical experiments, a relatively wet UTZ subjected to subduction stresses produces substantial radial anisotropy and about 1% azimuthal anisotropy (Figures 4a and 5a). Contrastingly, a fully dry UTZ appears mostly isotropic (Figures 4b and 5b). Relative to the dry UTZ model, the anisotropy distribution in the hydrous case is more consistent with source-side splitting observations surrounding deep earthquakes, particularly in the western Pacific (Mohiuddin et al., 2015; Nowacki et al., 2015) (Figure 6). Our predictions, however, are not perfect, particularly a_z where its amplitude appears underestimated. Around slabs, Moulík and Ekström (2014) measured radial anisotropy of about $\xi \sim 1.04$ underneath the circum-Pacific region; whereas azimuthal anisotropy could reach up to $a_z \sim 3\%$ according to Huang et al. (2019). There are several propositions for the increased anisotropy around subduction zones aside from wadsleyite CPO. Local enrichment of akimotoite may be the leading cause for source-side shear wave splitting observations underneath subduction zones (Foley & Long, 2011; Shiraishi et al., 2008). Dense hydrous magnesium silicates (DHMS) have also been shown to be very anisotropic at UTZ conditions (Nowacki et al., 2015) but their abundance and stability remain inconclusive (Hao et al., 2020). Although Nowacki et al. (2015) suggested SPO may contribute to the development of anisotropy, this may be unlikely since elliptical inclusions must be periodically aligned vertically to match $\xi < 1$ around subduction zones where horizontal laminations are more rampant instead (Faccenda et al., 2019; Magali et al., 2021). Furthermore, neither metastable olivine nor topotactical relationships between olivine and wadsleyite could be possible candidates due to their unlikely existence in hydrous environments (Smyth et al., 2012). It is thus plausible that the amount of effective strains in our models did not achieve that of actual subduction systems, and that our 2D setting relegates the complexity of deformation patterns which would explain the discrepancy in anisotropy strength (McKenzie, 1979). Even so, we assert that the patterns of UTZ anisotropy we predict remain robust.

The incorporation of water in wadsleyite promotes CPO development in light of our numerical experiments, and while its elastic properties also depend on water content, Magali, Ledoux, et al. (2024) and Ledoux, Saki, et al. (2023) demonstrated numerically that water also enhances the intrinsic anisotropy in its single crystal elastic tensor, and therefore contribute to the variability of anisotropy in the UTZ. This challenges the study of Chang and Ferreira (2019) where it is inferred that a dry UTZ is likely the cause of substantial radial anisotropy ($\xi \sim 1.02 - 1.03$) across slabs underneath the western Pacific. While a dry single crystal wadsleyite indeed contains larger intrinsic anisotropy, Zhou et al. (2022) reported anisotropy increases with water content in the case

of deformed wadsleyite aggregates, primarily due to increased crystallographic defects that weaken its rheology. With enough deformation accumulated in the UTZ, we model, for the first time, the dependence of the distribution of large-scale anisotropy on water. The relatively misunderstood effect of strong accumulation, however, precludes the prediction of anisotropy strength with the degree of hydration in the UTZ. Further analyses are imperative to reconcile seismic observations (e.g., Chang & Ferreira, 2019) and mineralogical experiments (e.g., Ohuchi et al., 2014; Zhou et al., 2022) with the help of additional constraints such as electrical conductivity measurements (Karato, 2011; Kelbert et al., 2009).

4.3. Comments on Intraslab Anisotropy

At a specific depth profile taken underneath the back-arc basin (Figures 7c and 8c), ξ^* and a_z^* both show near identical strength with respect to their observed counterparts, ξ_{obs} and a_z^{obs} , albeit shifted deeper by ~ 100 km. One plausible explanation for this difference could be attributed to the difference in the lithosphere-asthenosphere boundary (LAB) depth predicted from our thermochemical model, and the actual LAB depth underneath Honshu. Because CPO-induced anisotropy in the upper mantle is mostly confined beneath the plates where strains are presumed to be large, having LAB depth from past seismological studies (e.g., Nagumo & Junzo, 1988) as an added constraint would help correct for this shift in the depth distribution of anisotropy. Furthermore, while we allow for the computation of fabrics within the rigid slab, the amount of accumulated deformation is so small that the CPO within it remains random; hence, producing negligible seismic anisotropy. Previous work, however, based on receiver function inversion have suggested the presence of fossil fabrics as cause for intraslab anisotropy at shallow depths, particularly underneath the Nankai trough (Audet, 2013). Faccenda et al. (2008) suggested that since slabs are susceptible to hydration and faulting, a combination of CPO and shape preferred orientation (SPO) of serpentinized faults could also lead to noticeable intraslab anisotropy. Whether these are preserved within the slab in the deep upper mantle or in the mantle transition zone, however, still remains an open question due to transient deformation that complicate anisotropy patterns and concurrent issue regarding ill-constrained intraslab anisotropy. Fortunately enough, recent S-wave studies found evidence for intraslab anisotropy under mantle transition zone (Z. Zhang et al., 2024) and upper lower mantle conditions (Agrawal et al., 2020) in the Nazca subduction zone which have yet to be observed in other regions. Our models currently preclude frozen-in anisotropy within the slab, and while we acknowledge this could also help reconcile our model with observations at shallow depths, the same could not be said at mid-mantle depths due to disagreements of the predicted fast axis of fossil anisotropy and the observed shear wave splitting measurements (Agrawal et al., 2020).

5. Conclusion

We have integrated pressure(P)-induced olivine fabric transitions and P -induced phase transformations in CPO calculations to predict the distribution of large-scale anisotropy around a subduction zone. While contemporary studies interpret large-scale anisotropy in terms of the CPO of A-type olivine, we show that the variability of large-scale anisotropy that is lacking in an A-type model such as the localized $\xi < 1$ features observed in tomography can be emulated by a mantle model that incorporates P -induced olivine slip transitions. Strain partitioning, modeling of multi-phase aggregates, and implementations of other potential mechanisms for CPO development may not be warranted; reducing the number of free parameters that need to be constrained. In the upper transition zone (UTZ), the CPO of deformed hydrous wadsleyite is likely the leading cause for the observed anisotropy near the subducting slab. This opens a fresh perspective on how water is integral to its deformation history. Discrepancies in the strength of anisotropy, however, remain an open question. Further challenges therefore await such as identifying an empirical relationship between the amount of water and the strength of anisotropy in deformed aggregates.

Data Availability Statement

Subduction flow modeling and fabric calculations were performed using the open software ASPECT (Bangerth et al., 2024; Heister et al., 2017; Kronbichler et al., 2012) and VPSC, described in Lebensohn and Tomé (1993), respectively. The input files for Aspect and VPSC, useful routines for calculating single crystal elastic constants and CRSS as a function of P and T , and output elastic tensor files are available on Zenodo (Magali, Thomas, et al., 2024)—<https://zenodo.org/records/12774418>. The Fast Fourier Homogenization (FFH) code is based upon

Capdeville et al. (2015) and Capdeville and Métivier (2018) and available on Zenodo at Capdeville (2025)—
<https://zenodo.org/records/14640211>.

Acknowledgments

The study was funded by the bilateral ANR-DFG TIMEleSS project (ANR-17-CE31-0025) and by the DFG LASSIE project (TH 1530/18-1; SA 2585/3-1; SP1216/8-1; TH1530/24-1). Computations were primarily performed in the in-house PALMA cluster of the University of Münster. Preliminary simulations were also made possible thanks to the Zeus cluster of the University of Lille. We would like to thank the reviewers M. Faccenda and S. Agrawal, and the editor B. Kaus for the helpful comments that improved the quality of the manuscript.

References

- Agrawal, S., Eakin, C. M., Portner, D. E., Rodriguez, E. E., & Beck, S. L. (2020). The deformational journey of the Nazca slab from seismic anisotropy. *Geophysical Research Letters*, *47*(11), e2020GL087398. <https://doi.org/10.1029/2020gl087398>
- Agrusta, R., Goes, S., & Van Hunen, J. (2017). Subducting-slab transition-zone interaction: Stagnation, penetration and mode switches. *Earth and Planetary Science Letters*, *464*, 10–23. <https://doi.org/10.1016/j.epsl.2017.02.005>
- Allègre, C. J., & Turcotte, D. L. (1986). Implications of a two-component marble-cake mantle. *Nature*, *323*(6084), 123–127. <https://doi.org/10.1038/323123a0>
- Audet, P. (2013). Seismic anisotropy of subducting oceanic uppermost mantle from fossil spreading. *Geophysical Research Letters*, *40*(1), 173–177. <https://doi.org/10.1029/2012gl054328>
- Bangerth, W., Dannberg, J., Fraters, M., Gassmoeller, R., Glerum, A., Heister, T., et al. (2024). Aspect v3.0.0 [Software]. *Zenodo*. <https://doi.org/10.5281/zenodo.14371679>
- Becker, T. W., Kellogg, J. B., Ekström, G., & O'Connell, R. J. (2003). Comparison of azimuthal seismic anisotropy from surface waves and finite strain from global mantle-circulation models. *Geophysical Journal International*, *155*(2), 696–714. <https://doi.org/10.1046/j.1365-246x.2003.02085.x>
- Becker, T. W., & Lebedev, S. (2021). Dynamics of the upper mantle in light of seismic anisotropy. In H. Marquardt, M. Ballmer, S. Cottar, & J. Konter (Eds.), *Mantle convection and surface expressions* (pp. 257–282). Wiley Online Library. <https://doi.org/10.1002/9781119528609.ch10>
- Bercovici, D., & Karato, S.-I. (2003). Whole-mantle convection and the transition-zone water filter. *Nature*, *425*(6953), 39–44. <https://doi.org/10.1038/nature01918>
- Bernard, R. E., Behr, W. M., Becker, T. W., & Young, D. J. (2019). Relationships between olivine CPO and deformation parameters in naturally deformed rocks and implications for mantle seismic anisotropy. *Geochemistry, Geophysics, Geosystems*, *20*(7), 3469–3494. <https://doi.org/10.1029/2019GC008289>
- Burgos, G., Montagner, J.-P., Beucler, E., Capdeville, Y., Mocquet, A., & Drilleau, M. (2014). Oceanic lithosphere-asthenosphere boundary from surface wave dispersion data. *Journal of Geophysical Research: Solid Earth*, *119*(2), 1079–1093. <https://doi.org/10.1002/2013jb010528>
- Capdeville, Y. (2025). homofft [Software]. *Zenodo*. <https://doi.org/10.5281/ZENODO.14640211>
- Capdeville, Y., Guillot, L., & Marigo, J.-J. (2010). 2-d non-periodic homogenization to upscale elastic media for P-SV waves. *Geophysical Journal International*, *182*(2), 903–922. <https://doi.org/10.1111/j.1365-246x.2010.04636.x>
- Capdeville, Y., & Métivier, L. (2018). Elastic full waveform inversion based on the homogenization method: Theoretical framework and 2-d numerical illustrations. *Geophysical Journal International*, *213*(2), 1093–1112. <https://doi.org/10.1093/gji/ggy039>
- Capdeville, Y., Zhao, M., & Cupillard, P. (2015). Fast Fourier homogenization for elastic wave propagation in complex media. *Wave Motion*, *54*, 170–186. <https://doi.org/10.1016/j.wavemoti.2014.12.006>
- Castelnau, O., Blackman, D., Lebensohn, R., & Ponte Castañeda, P. (2008). Micromechanical modeling of the viscoplastic behavior of olivine. *Journal of Geophysical Research*, *113*(B9), B09202. <https://doi.org/10.1029/2007jb005444>
- Chang, S.-J., Ferreira, A. M. G., Ritsema, J., van Heijst, H. J., & Woodhouse, J. H. (2015). Joint inversion for global isotropic and radially anisotropic mantle structure including crustal thickness perturbations. *Journal of Geophysical Research: Solid Earth*, *120*(6), 4278–4300. <https://doi.org/10.1002/2014jb011824>
- Chang, S.-J., & Ferreira, A. M. (2019). Inference on water content in the mantle transition zone near subducted slabs from anisotropy tomography. *Geochemistry, Geophysics, Geosystems*, *20*(2), 1189–1201. <https://doi.org/10.1029/2018gc008090>
- Connolly, J. A. (2005). Computation of phase equilibria by linear programming: A tool for geodynamic modeling and its application to subduction zone decarbonation. *Earth and Planetary Science Letters*, *236*(1–2), 524–541. <https://doi.org/10.1016/j.epsl.2005.04.033>
- Connolly, J. A. (2009). The geodynamic equation of state: What and how. *Geochemistry, Geophysics, Geosystems*, *10*(10), Q10014. <https://doi.org/10.1029/2009gc002540>
- Debayle, E., Dubuffet, F., & Durand, S. (2016). An automatically updated S-wave model of the upper mantle and the depth extent of azimuthal anisotropy. *Geophysical Research Letters*, *43*(2), 674–682. <https://doi.org/10.1002/2015GL067329>
- Durinck, J., Carrez, P., & Cordier, P. (2007). Application of the Peierls-Nabarro model to dislocations in forsterite. *European Journal of Mineralogy*, *19*(5), 631–639. <https://doi.org/10.1127/0935-1221/2007/0019-1757>
- Dziewonski, A. M., & Anderson, D. L. (1981). Preliminary reference Earth model. *Physics of the Earth and Planetary Interiors*, *25*(4), 297–356. [https://doi.org/10.1016/0031-9201\(81\)90046-7](https://doi.org/10.1016/0031-9201(81)90046-7)
- Faccenda, M. (2014). Mid mantle seismic anisotropy around subduction zones. *Physics of the Earth and Planetary Interiors*, *227*, 1–19. <https://doi.org/10.1016/j.pepi.2013.11.015>
- Faccenda, M., Burlini, L., Gerya, T. V., & Mainprice, D. (2008). Fault-induced seismic anisotropy by hydration in subducting oceanic plates. *Nature*, *455*(7216), 1097–1100. <https://doi.org/10.1038/nature07376>
- Faccenda, M., & Capitanio, F. A. (2012). Development of mantle seismic anisotropy during subduction-induced 3-d flow. *Geophysical Research Letters*, *39*(11), L11305. <https://doi.org/10.1029/2012gl051988>
- Faccenda, M., & Capitanio, F. A. (2013). Seismic anisotropy around subduction zones: Insights from three-dimensional modeling of upper mantle deformation and SKS splitting calculations. *Geochemistry, Geophysics, Geosystems*, *14*(1), 243–262. <https://doi.org/10.1002/ggge.20055>
- Faccenda, M., Ferreira, A. M., Tisato, N., Lithgow-Bertelloni, C., Stixrude, L., & Pennacchioni, G. (2019). Extrinsic elastic anisotropy in a compositionally heterogeneous Earth's mantle. *Journal of Geophysical Research: Solid Earth*, *124*(2), 1671–1687. <https://doi.org/10.1029/2018jb016482>
- Ferreira, A. M., Faccenda, M., Sturgeon, W., Chang, S.-J., & Schardong, L. (2019). Ubiquitous lower-mantle anisotropy beneath subduction zones. *Nature Geoscience*, *12*(4), 301–306. <https://doi.org/10.1038/s41561-019-0325-7>
- Foley, B. J., & Long, M. D. (2011). Upper and mid-mantle anisotropy beneath the Tonga slab. *Geophysical Research Letters*, *38*(2), L02303. <https://doi.org/10.1029/2010gl046021>
- Fraters, M. R. T., & Billen, M. I. (2021). On the implementation and usability of crystal preferred orientation evolution in geodynamic modeling. *Geochemistry, Geophysics, Geosystems*, *22*(10), e2021GC009846. <https://doi.org/10.1029/2021GC009846>
- French, S., & Romanowicz, B. A. (2014). Whole-mantle radially anisotropic shear velocity structure from spectral-element waveform tomography. *Geophysical Journal International*, *199*(3), 1303–1327. <https://doi.org/10.1093/gji/ggu334>

- Fukao, Y., & Obayashi, M. (2013). Subducted slabs stagnant above, penetrating through, and trapped below the 660 km discontinuity. *Journal of Geophysical Research: Solid Earth*, *118*(11), 5920–5938. <https://doi.org/10.1002/2013JB010466>
- Gay, J. P., Ledoux, E. E., Krug, M., Chantel, J., Pakhomova, A., Sanchez-Valle, C., et al. (2024). Depth dependent deformation and anisotropy of pyrolyte in the Earth's lower mantle. *Geophysical Research Letters*, *51*(11), e2024GL109433. <https://doi.org/10.1029/2024gl109433>
- Glerum, A., Thieulot, C., Fraters, M., Blom, C., & Spakman, W. (2018). Nonlinear viscoplasticity in aspect: Benchmarking and applications to subduction. *Solid Earth*, *9*(2), 267–294. <https://doi.org/10.5194/se-9-267-2018>
- Goes, S., Agrusta, R., van Hunen, J., & Garel, F. (2017). Subduction-transition zone interaction: A review. *Geosphere*, *13*(3), 644–664. <https://doi.org/10.1130/ges01476.1>
- Hao, M., Zhang, J. S., Pierotti, C. E., Zhou, W.-Y., Zhang, D., & Dera, P. (2020). The seismically fastest chemical heterogeneity in the Earth's deep upper mantle—Implications from the single-crystal thermoelastic properties of jadeite. *Earth and Planetary Science Letters*, *543*, 116345. <https://doi.org/10.1016/j.epsl.2020.116345>
- Heister, T., Dannberg, J., Gassmüller, R., & Bangerth, W. (2017). High accuracy mantle convection simulation through modern numerical methods. II: Realistic models and problems. *Geophysical Journal International*, *210*(2), 833–851. <https://doi.org/10.1093/gji/ggx195>
- Hirth, G., & Kohlstedt, D. (2003). Rheology of the upper mantle and the mantle wedge: A view from the experimentalists. In J. Eiler (Ed.), *Inside the subduction factory cover image inside the subduction factory* (Vol. 138, pp. 83–105). American Geophysical Union. <https://doi.org/10.1029/138gm06>
- Honda, S., & Yoshida, T. (2005). Application of the model of small-scale convection under the island arc to the NE Honshu subduction zone. *Geochemistry, Geophysics, Geosystems*, *6*(1). <https://doi.org/10.1029/2004GC000785>
- Huang, Q., Schmerr, N., Waszek, L., & Beghein, C. (2019). Constraints on seismic anisotropy in the mantle transition zone from long-period SS precursors. *Journal of Geophysical Research: Solid Earth*, *124*(7), 6779–6800. <https://doi.org/10.1029/2019jb017307>
- Jung, H., Mo, W., & Green, H. W. (2009). Upper mantle seismic anisotropy resulting from pressure-induced slip transition in olivine. *Nature Geoscience*, *2*(1), 73–77. <https://doi.org/10.1038/ngeo389>
- Kaminski, E., Ribe, N. M., & Browaeys, J. T. (2004). D-rax, a program for calculation of seismic anisotropy due to crystal lattice preferred orientation in the convective upper mantle. *Geophysical Journal International*, *158*(2), 744–752. <https://doi.org/10.1111/j.1365-246x.2004.02308.x>
- Karato, S.-I. (1998). Seismic anisotropy in the deep mantle, boundary layers and the geometry of mantle convection. In *Geodynamics of lithosphere & Earth's mantle* (pp. 565–587). Springer. https://doi.org/10.1007/978-3-0348-8777-9_19
- Karato, S.-I. (2011). Water distribution across the mantle transition zone and its implications for global material circulation. *Earth and Planetary Science Letters*, *301*(3–4), 413–423. <https://doi.org/10.1016/j.epsl.2010.11.038>
- Karato, S.-I., Jung, H., Katayama, I., & Skemer, P. (2008). Geodynamic significance of seismic anisotropy of the upper mantle: New insights from laboratory studies. *Annual Review of Earth and Planetary Sciences*, *36*(1), 59–95. <https://doi.org/10.1146/annurev.earth.36.031207.124120>
- Karato, S.-I., & Wu, P. (1993). Rheology of the upper mantle: A synthesis. *Science*, *260*(5109), 771–778. <https://doi.org/10.1126/science.260.5109.771>
- Katayama, I., & ichiro Karato, S. (2006). Effect of temperature on the b- to c-type olivine fabric transition and implication for flow pattern in subduction zones. *Physics of the Earth and Planetary Interiors*, *157*(1), 33–45. <https://doi.org/10.1016/j.pepi.2006.03.005>
- Katayama, I., Jung, H., & Karato, S.-I. (2004). New type of olivine fabric from deformation experiments at modest water content and low stress. *Geology*, *32*(12), 1045–1048. <https://doi.org/10.1130/g20805.1>
- Kawazoe, T., Ohuchi, T., Nishihara, Y., Nishiyama, N., Fujino, K., & Irifune, T. (2013). Seismic anisotropy in the mantle transition zone induced by shear deformation of wadsleyite. *Physics of the Earth and Planetary Interiors*, *216*, 91–98. <https://doi.org/10.1016/j.pepi.2012.12.005>
- Kelbert, A., Schultz, A., & Egbert, G. (2009). Global electromagnetic induction constraints on transition-zone water content variations. *Nature*, *460*(7258), 1003–1006. <https://doi.org/10.1038/nature08257>
- Kendall, E., Faccenda, M., Ferreira, A., & Chang, S.-J. (2022). On the relationship between oceanic plate speed, tectonic stress, and seismic anisotropy. *Geophysical Research Letters*, *49*(15), e2022GL097795. <https://doi.org/10.1029/2022gl097795>
- Kneller, E. A., van Keken, P. E., Katayama, I., & Karato, S. (2007). Stress, strain, and b-type olivine fabric in the fore-arc mantle: Sensitivity tests using high-resolution steady-state subduction zone models. *Journal of Geophysical Research*, *112*(B4). <https://doi.org/10.1029/2006JB004544>
- Kronbichler, M., Heister, T., & Bangerth, W. (2012). High accuracy mantle convection simulation through modern numerical methods. *Geophysical Journal International*, *191*(1), 12–29. <https://doi.org/10.1111/j.1365-246x.2012.05609.x>
- Kumazawa, M., & Anderson, O. L. (1969). Elastic moduli, pressure derivatives, and temperature derivatives of single-crystal olivine and single-crystal forsterite. *Journal of Geophysical Research*, *74*(25), 5961–5972. <https://doi.org/10.1029/jb074i025p05961>
- Lebensohn, R. A., & Tomé, C. (1993). A self-consistent anisotropic approach for the simulation of plastic deformation and texture development of polycrystals: Application to zirconium alloys. *Acta Metallurgica et Materialia*, *41*(9), 2611–2624. [https://doi.org/10.1016/0956-7151\(93\)90130-k](https://doi.org/10.1016/0956-7151(93)90130-k)
- Ledoux, E. E., Krug, M., Gay, J., Chantel, J., Hilaret, N., Bykov, M., et al. (2023). In-situ study of microstructures induced by the olivine to wadsleyite transformation at conditions of the 410 km depth discontinuity. *American Mineralogist*, *108*(12), 2283–2293. <https://doi.org/10.2138/am-2022-8731>
- Ledoux, E. E., Saki, M., Gay, J. P., Krug, M., Castelnau, O., Zhou, W.-Y., et al. (2023). Deformation mechanisms, microstructures, and seismic anisotropy of wadsleyite in the Earth's transition zone. *Geochemistry, Geophysics, Geosystems*, *24*(11), e2023GC011026. <https://doi.org/10.1029/2023GC011026>
- Li, Z. H., Di Leo, J. F., & Ribe, N. M. (2014). Subduction-induced mantle flow, finite strain, and seismic anisotropy: Numerical modeling. *Journal of Geophysical Research: Solid Earth*, *119*(6), 5052–5076. <https://doi.org/10.1002/2014jb010996>
- Long, M. D., & Becker, T. W. (2010). Mantle dynamics and seismic anisotropy. *Earth and Planetary Science Letters*, *297*(3–4), 341–354. <https://doi.org/10.1016/j.epsl.2010.06.036>
- Long, M. D., & Silver, P. G. (2009). Shear wave splitting and mantle anisotropy: Measurements, interpretations, and new directions. *Surveys in Geophysics*, *30*(4–5), 407–461. <https://doi.org/10.1007/s10712-009-9075-1>
- Magali, J. K., Bodin, T., Hedjazian, N., Ricard, Y., Capdeville, Y., & Debayle, E. (2021). Quantifying intrinsic and extrinsic contributions to radial anisotropy in tomographic models. *Journal of Geophysical Research: Solid Earth*, *126*(10), e2021JB022322. <https://doi.org/10.1029/2021jb022322>
- Magali, J. K., Ledoux, E. E., Thomas, C., Capdeville, Y., & Merkel, S. (2024). Pressure-dependent large-scale seismic anisotropy induced by non-Newtonian mantle flow. *Geophysical Journal International*, *238*(1), 400–419. <https://doi.org/10.1093/gji/ggae165>
- Magali, J. K., Thomas, C., Ledoux, E. E., Capdeville, Y., & Merkel, S. (2024). Data supporting “on the influence of pressure, phase transitions, and water on large-scale seismic anisotropy underneath a subduction zone” [Dataset]. *Zenodo*. <https://doi.org/10.5281/ZENODO.12774418>

- Mainprice, D. (2007). Seismic anisotropy of the deep Earth from a mineral and rock physics perspective. In *Treatise on Geophysics* (Vol. 2, pp. 437–491). Elsevier. <https://doi.org/10.1016/B978-044452748-6.00045-6>
- Mainprice, D., Tommasi, A., Couvy, H., Cordier, P., & Frost, D. J. (2005). Pressure sensitivity of olivine slip systems and seismic anisotropy of Earth's upper mantle. *Nature*, *433*(7027), 731–733. <https://doi.org/10.1038/nature03266>
- McKenzie, D. (1979). Finite deformation during fluid flow. *Geophysical Journal International*, *58*(3), 689–715. <https://doi.org/10.1111/j.1365-246x.1979.tb04803.x>
- Mohiuddin, A., Long, M. D., & Lynner, C. (2015). Mid-mantle seismic anisotropy beneath southwestern Pacific subduction systems and implications for mid-mantle deformation. *Physics of the Earth and Planetary Interiors*, *245*, 1–14. <https://doi.org/10.1016/j.pepi.2015.05.003>
- Montagner, J.-P. (1998). Where can seismic anisotropy be detected in the Earth's mantle? In boundary layers. *Pure and Applied Geophysics*, *151*(2), 223–256. https://doi.org/10.1007/978-3-0348-8777-9_2
- Montagner, J.-P., Burgos, G., Capdeville, Y., Beucler, E., & Mocquet, A. (2021). The mantle transition zone dynamics as revealed through seismic anisotropy. *Tectonophysics*, *821*, 229133. <https://doi.org/10.1016/j.tecto.2021.229133>
- Montagner, J.-P., & Nataf, H.-C. (1986). A simple method for inverting the azimuthal anisotropy of surface waves. *Journal of Geophysical Research*, *91*(B1), 511–520. <https://doi.org/10.1029/jb091ib01p00511>
- Moulik, P., & Ekström, G. (2014). An anisotropic shear velocity model of the Earth's mantle using normal modes, body waves, surface waves and long-period waveforms. *Geophysical Journal International*, *199*(3), 1713–1738. <https://doi.org/10.1093/gji/ggu356>
- Nagumo, S., & Junzo, K. (1988). The P-wave structure of the lithosphere-asthenosphere in the western Pacific: A comparison of ocean versus continent. *Tectonophysics*, *147*(1–2), 85–93. [https://doi.org/10.1016/0040-1951\(88\)90149-7](https://doi.org/10.1016/0040-1951(88)90149-7)
- Nanjo, K., Ishibe, T., Tsuruoka, H., Schorlemmer, D., Ishigaki, Y., & Hirata, N. (2010). Analysis of the completeness magnitude and seismic network coverage of Japan. *Bulletin of the Seismological Society of America*, *100*(6), 3261–3268. <https://doi.org/10.1785/0120100077>
- Nettles, M., & Dziewoński, A. M. (2008). Radially anisotropic shear velocity structure of the upper mantle globally and beneath north America. *Journal of Geophysical Research*, *113*(B2), B02303. <https://doi.org/10.1029/2006jb004819>
- Nowacki, A., Kendall, J.-M., Wookey, J., & Pemberton, A. (2015). Mid-mantle anisotropy in subduction zones and deep water transport. *Geochemistry, Geophysics, Geosystems*, *16*(3), 764–784. <https://doi.org/10.1002/2014gc005567>
- Núñez-Valdez, M., Wu, Z., Yu, Y., & Wentzcovitch, R. (2013). Thermal elasticity of (Fe_xMg_{1-x})₂SiO₄ olivine and wadsleyite. *Geophysical Research Letters*, *40*(2), 290–294. <https://doi.org/10.1002/grl.50131>
- Ohuchi, T., Fujino, K., Kawazoe, T., & Irifune, T. (2014). Crystallographic preferred orientation of wadsleyite and ringwoodite: Effects of phase transformation and water on seismic anisotropy in the mantle transition zone. *Earth and Planetary Science Letters*, *397*, 133–144. <https://doi.org/10.1016/j.epsl.2014.03.066>
- Ohuchi, T., Kawazoe, T., Nishihara, Y., & Irifune, T. (2012). Change of olivine a-axis alignment induced by water: Origin of seismic anisotropy in subduction zones. *Earth and Planetary Science Letters*, *317–318*, 111–119. <https://doi.org/10.1016/j.epsl.2011.11.022>
- Ohuchi, T., Kawazoe, T., Nishihara, Y., Nishiyama, N., & Irifune, T. (2011). High pressure and temperature fabric transitions in olivine and variations in upper mantle seismic anisotropy. *Earth and Planetary Science Letters*, *304*(1–2), 55–63. <https://doi.org/10.1016/j.epsl.2011.01.015>
- Panning, M., & Romanowicz, B. (2006). A three-dimensional radially anisotropic model of shear velocity in the whole mantle. *Geophysical Journal International*, *167*(1), 361–379. <https://doi.org/10.1111/j.1365-246x.2006.03100.x>
- Piromallo, C., Becker, T., Funicello, F., & Faccenna, C. (2006). Three-dimensional instantaneous mantle flow induced by subduction. *Geophysical Research Letters*, *33*(8). <https://doi.org/10.1029/2005gl025390>
- Raterron, P., Chen, J., Li, L., Weidner, D., & Cordier, P. (2007). Pressure-induced slip-system transition in forsterite: Single-crystal rheological properties at mantle pressure and temperature. *American Mineralogist*, *92*(8–9), 1436–1445. <https://doi.org/10.2138/am.2007.2474>
- Raterron, P., Detrez, F., Castelnaud, O., Bollinger, C., Cordier, P., & Merkel, S. (2014). Multiscale modeling of upper mantle plasticity: From single-crystal rheology to multiphase aggregate deformation. *Physics of the Earth and Planetary Interiors*, *228*, 232–243. <https://doi.org/10.1016/j.pepi.2013.11.012>
- Raterron, P., Girard, J., & Chen, J. (2012). Activities of olivine slip systems in the upper mantle. *Physics of the Earth and Planetary Interiors*, *200–201*, 105–112. <https://doi.org/10.1016/j.pepi.2012.04.006>
- Ringwood, A. E. (1991). Phase transformations and their bearing on the constitution and dynamics of the mantle. *Geochimica et Cosmochimica Acta*, *55*(8), 2083–2110. [https://doi.org/10.1016/0016-7037\(91\)90090-r](https://doi.org/10.1016/0016-7037(91)90090-r)
- Rychert, C. A., Schmerr, N., & Harmon, N. (2012). The Pacific lithosphere-asthenosphere boundary: Seismic imaging and anisotropic constraints from SS waveforms. *Geochemistry, Geophysics, Geosystems*, *13*(9), Q0AK10. <https://doi.org/10.1029/2012GC004194>
- Sato, H., Iwasaki, T., Kawasaki, S., Ikeda, Y., Matsuta, N., Takeda, T., et al. (2004). Formation and shortening deformation of a back-arc rift basin revealed by deep seismic profiling, central Japan. *Tectonophysics*, *388*(1–4), 47–58. <https://doi.org/10.1016/j.tecto.2004.07.004>
- Schubert, G., Turcotte, D. L., & Olson, P. (2001). *Mantle convection in the Earth and planets*. Cambridge University Press. <https://doi.org/10.1017/CBO9780511612879>
- Shiraishi, R., Ohtani, E., Kanagawa, K., Shimoyuku, A., & Zhao, D. (2008). Crystallographic preferred orientation of akimotoite and seismic anisotropy of Tonga slab. *Nature*, *455*(7213), 657–660. <https://doi.org/10.1038/nature07301>
- Simmons, N. A., Myers, S., Morency, C., Chiang, A., & Knapp, D. (2021). Spiral: A multiresolution global tomography model of seismic wave speeds and radial anisotropy variations in the crust and mantle. *Geophysical Journal International*, *227*(2), 1366–1391. <https://doi.org/10.1093/gji/ggab277>
- Simmons, N. A., Schuberth, B. S., Myers, S. C., & Knapp, D. R. (2019). Resolution and covariance of the LLNL-G3D-JPS global seismic tomography model: Applications to travel time uncertainty and tomographic filtering of geodynamic models. *Geophysical Journal International*, *217*(3), 1543–1557. <https://doi.org/10.1093/gji/ggz102>
- Smith, M. L., & Dahlen, F. (1973). The azimuthal dependence of love and Rayleigh wave propagation in a slightly anisotropic medium. *Journal of Geophysical Research*, *78*(17), 3321–3333. <https://doi.org/10.1029/jb078i017p03321>
- Smyth, J. R., Miyajima, N., Huss, G. R., Hellebrand, E., Rubie, D. C., & Frost, D. J. (2012). Olivine–wadsleyite–pyroxene topotaxy: Evidence for coherent nucleation and diffusion-controlled growth at the 410-km discontinuity. *Physics of the Earth and Planetary Interiors*, *200–201*, 85–91. <https://doi.org/10.1016/j.pepi.2012.04.003>
- Stixrude, L., & Lithgow-Bertelloni, C. (2022). Thermal expansivity, heat capacity and bulk modulus of the mantle. *Geophysical Journal International*, *228*(2), 1119–1149. <https://doi.org/10.1093/gji/ggab394>
- Sturgeon, W., Ferreira, A. M., Faccenda, M., Chang, S.-J., & Scharndong, L. (2019). On the origin of radial anisotropy near subducted slabs in the midmantle. *Geochemistry, Geophysics, Geosystems*, *20*(11), 5105–5125. <https://doi.org/10.1029/2019gc008462>

- Vauchez, A., & Garrido, C. J. (2001). Seismic properties of an asthenospherized lithospheric mantle: Constraints from lattice preferred orientations in peridotite from the Ronda massif. *Earth and Planetary Science Letters*, *192*(2), 235–249. [https://doi.org/10.1016/s0012-821x\(01\)00448-4](https://doi.org/10.1016/s0012-821x(01)00448-4)
- Wakita, K. (2018). Geology of the Japanese Islands: An outline. In *Natural Heritage of Japan: Geological, Geomorphological, and Ecological Aspects* (pp. 9–17).
- Wenk, H.-R., & Tomé, C. N. (1999). Modeling dynamic recrystallization of olivine aggregates deformed in simple shear. *Journal of Geophysical Research*, *104*(B11), 25513–25527. <https://doi.org/10.1029/1999jb900261>
- Yuan, K., & Beghein, C. (2013). Seismic anisotropy changes across upper mantle phase transitions. *Earth and Planetary Science Letters*, *374*, 132–144. <https://doi.org/10.1016/j.epsl.2013.05.031>
- Zhang, S., & Karato, S.-I. (1995). Lattice preferred orientation of olivine aggregates deformed in simple shear. *Nature*, *375*(6534), 774–777. <https://doi.org/10.1038/375774a0>
- Zhang, Z., Yu, W.-C., & Huang, H.-H. (2024). Constraining seismic anisotropy on the mantle transition zone boundaries beneath the subducting Nazca slab. *Physics of the Earth and Planetary Interiors*, *350*, 107179. <https://doi.org/10.1016/j.pepi.2024.107179>
- Zhou, W.-Y., Hao, M., Zhang, J. S., Chen, B., Wang, R., & Schmandt, B. (2022). Constraining composition and temperature variations in the mantle transition zone. *Nature Communications*, *13*, 1–9. <https://doi.org/10.1038/s41467-022-28709-7>
- Zimmerman, M. E., Zhang, S., Kohlstedt, D. L., & Karato, S.-I. (1999). Melt distribution in mantle rocks deformed in shear. *Geophysical Research Letters*, *26*(10), 1505–1508. <https://doi.org/10.1029/1999gl900259>